Materials Today Physics 21 (2021) 100548

Contents lists available at ScienceDirect

Materials Today Physics

journal homepage: https://www.journals.elsevier.com/materials-today-physics

Quasiparticle twist dynamics in non-symmorphic materials

R. Juneja [a], S. Thébaud [a], T. Pandey [a, b], C.A. Polanco [a], D.H. Moseley [a], M.E. Manley [a], Y.Q. Cheng [c], B. Winn [c], D.L. Abernathy [c], R.P. Hermann [a, **, 2], L. Lindsay [a, *, 1]

[a] Materials Science and Technology Division, Oak Ridge National Laboratory, Oak Ridge, TN, 37831, USA
[b] Department of Physics, University of Antwerp-B2020, Belgium
[c] Neutron Scattering Division, Oak Ridge National Laboratory, Oak Ridge, TN, 37831, USA

ARTICLE INFO

Article history:
Received 4 August 2021
Received in revised form
7 September 2021
Accepted 24 September 2021
Available online 30 September 2021

Keywords:
Lattice dynamics
Chiral quasiparticles
Neutron scattering
Tellurium dioxide
Thermal transport

ABSTRACT

Quasiparticle physics underlies our understanding of the microscopic dynamical behaviors of materials that govern a vast array of properties, including structural stability, excited states and interactions, dynamical structure factors, and electron and phonon conductivities. Thus, understanding band structures and quasiparticle interactions is foundational to the study of condensed matter. Here we advance a 'twist' dynamical description of quasiparticles (including phonons and Bloch electrons) in non-symmorphic chiral and achiral materials. Such materials often have structural complexity, strong thermal resistance, and efficient thermoelectric performance for waste heat capture and clean refrigeration technologies. The twist dynamics presented here provides a novel perspective of quasiparticle behaviors in such complex materials, in particular highlighting how non-symmorphic symmetries determine band crossings and anti-crossings, topological behaviors, quasiparticle interactions that govern transport, and observables in scattering experiments. We provide specific context via neutron scattering measurements and first-principles calculations of phonons and electrons in chiral tellurium dioxide. Building twist symmetries into the quasiparticle dynamics of non-symmorphic materials offers intuition into quasiparticle behaviors, materials properties, and guides improved experimental designs to probe them. More specifically, insights into the phonon and electron quasiparticle physics presented here will enable materials design strategies to control interactions and transport for enhanced thermoelectric and thermal management applications.

1. Introduction

Structural twisting underlies a variety of profoundly important concepts in biological and condensed matter systems, from genetic information in double helix DNA [1,2] to superconductivity in twisted bilayer graphene [3,4]. Microscopic quasiparticle excitations that determine materials behaviors (*e.g.*, phonons, Bloch electrons) are fundamentally governed by structural twist in chiral and achiral systems [5,6], with a large subset of these having non-symmorphic symmetry elements, *i.e.*, having screw axes or glide planes [7,8]. Here, we examine crystals with quantized rotational symmetries – layers related by $2\pi/n$ rotations with n an integer. This is not to be confused with the burgeoning physics of bilayer Moiré materials that take on continuous twist angles between two monolayers [3,4]. We show that non-symmorphic twist symmetries dictate quasiparticle behaviors including quantum phase interference conditions (*i.e.*, conservation of pseudoangular momentum) [9–14], symmetry-enforced crossings and anti-crossings [6,15–19], and topological classifications [19–29] that can have profound effects on global material properties, such as spectral observables and electronic and thermal transport. Furthermore, many non-symmorphic materials have complex unit cells, which are often favorable for thermoelectric applications that require large vibrational thermal resistance as structural complexity leads to strong scattering of heat-carrying phonons. Chiral and achiral non-symmorphic materials of interest for such applications include: elemental Te [30], Zintl-phase chiral clathrates [31], $Ba_6Sn_6Se_{13}$ [32], In_5Se_5Br [33], and BiCuSeO [34]. This work

* Corresponding author.
** Corresponding author.
E-mail addresses: hermannrp@ornl.gov (R.P. Hermann), lindsaylr@ornl.gov (L. Lindsay).
[1] Theory.
[2] Experiment.

https://doi.org/10.1016/j.mtphys.2021.100548

demonstrates that in such materials non-symmorphic twist symmetries underly phonon band anti-crossings and topological behaviors in chiral variants, both associated with low thermal conductivity and good thermoelectric performance [35–38]. Twist symmetries also govern quantum phase interference conditions that determine electron and phonon interactions, and thus thermoelectric properties.

2. Methods

Here we introduce a dynamics that exploits the twist symmetries of non-symmorphic materials to draw out novel interpretations of quasiparticle behaviors directly from dynamical phases. Accordingly, we identify a twist axis in a non-symmorphic material and break the primitive unit cell into smaller subunits related by internal symmetries (see Fig. 1a). Each subunit belongs to a layer of atoms (h) with translational periodicity perpendicular to the twist axis. We relabel the atoms in each layer by lattice vector $\vec{R} = (R_h, \theta_h)$ where R_h is the location of the hth layer along the twist axis with rotational orientation θ_h about the axis (R_h and θ_h are not independent).

2.1. Theory

Phonons in this twist basis are described by the dynamical matrix [10,11,32,39]:

$$\overline{D}_l = D^{kk'}_{\alpha\beta}(q,l) = \frac{1}{\sqrt{m_k m_{k'}}} \sum_{\gamma h' p'} \Phi^{0k,h'p'k'}_{\alpha\gamma} S_{\gamma\beta}(\theta_{h'}) e^{iqR_{h'}} e^{il\theta_{h'}} \quad (1)$$

where k labels atoms in the smaller subunits, m_k is the mass of the kth atom, Greek subscripts are Cartesian directions, $\Phi^{0k,h'p'k'}_{\alpha\beta}$ are harmonic force constants between atom k in the origin unit cell and atom k' in the h' layer in the p' unit cell (labeling cells perpendicular to the twist axis), and $S_{\alpha\beta}(\theta_h)$ is a rotation operator. Interactions perpendicular to the twist axis are included in the dynamics, though phases perpendicular to this axis are not relevant. In this formalism, the phonon wavevector has two components: a continuous translational wavevector q along the twist axis and a quantized pseudoangular momentum l corresponding to rotational phase around this axis. The range of l is determined by the number of unique twist operations along the axis. For each q and l, Eq. (1) is diagonalized to determine the phonon dispersion. Eq. (1) does not apply to points off the twist axis since the eigenmotions of the separate subunits are then not simply related by the twist phase symmetry. For spinless electrons, twist band dynamics can be similarly defined and is described in the Supplemental Materials (SM) for a tight-binding representation [40] built from density functional theory (DFT) calculations [41,42]. In this way, an electron twist Hamiltonian gives electronic band energies with similar pseudoangular momentum dependence. In the presence of spin-orbit coupling, the spin degree of freedom must be added to the pseudoangular momentum, while phonons remain unchanged (see Figs. S3(b) and S4 in the SM).

This formalism yields band structures identical to conventional dynamics, though interpreted in light of the twist phases carried by the quasiparticles. It can be generally applied to quasiparticle bands in non-symmorphic chiral and achiral materials determined from DFT calculations or model Hamiltonians. We note that a large variety of space groups support chiral and achiral materials with twists and screws, *e.g.*, $P2_1$, $P3_1$, $P4_1$, and $P6_1$ with two-, three-, four-, and six-fold rotations. Twist dynamics builds insights into quasiparticle behaviors governed by combinations of rotational phase factors $e^{il\theta_h}$, including quasiparticle interactions, symmetry-enforced crossings and topologies in band structures, and

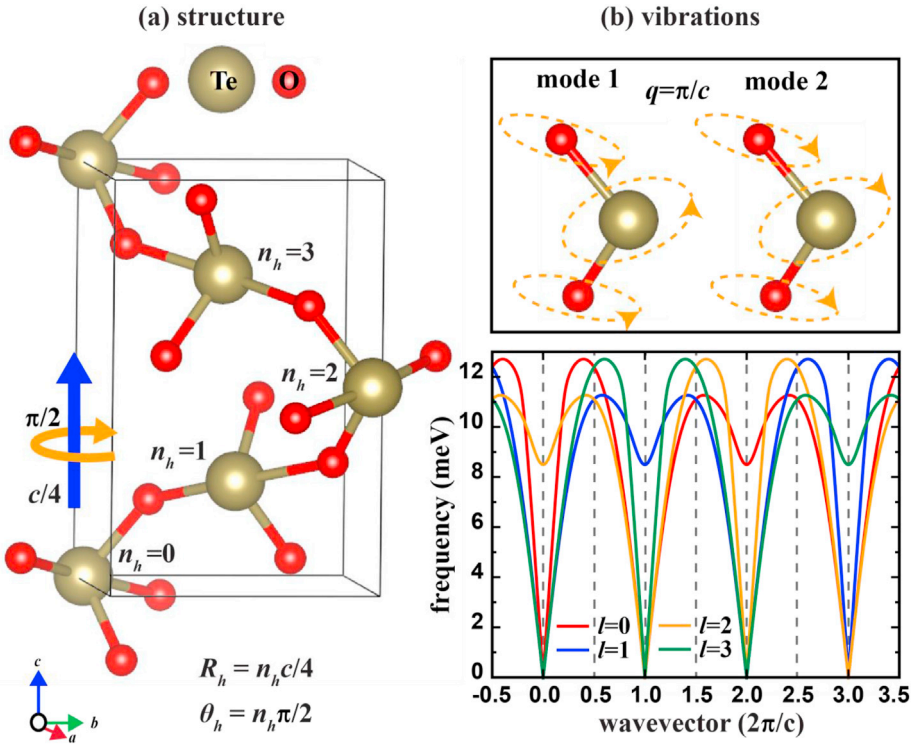

Fig. 1. **(a)** Structure of α-TeO_2 demonstrating the chiral symmetry along the c-axis. Each TeO_2 unit (O atoms from other cells are also shown) represents a layer of atoms periodic along a and b axes. Each layer is related by a $c/4$ translation and $\pi/2$ rotation. **(b) upper panel:** Opposite chiral vibrations of a subset of TeO_2 atoms at a crossing of complex conjugate pairs at the BZ boundary. **(b) lower panel:** Low frequency phonon dispersion over multiple BZs of α-TeO_2 along the chiral c-axis with bands color-coded by their pseudoangular momentum l. (For interpretation of the references to color in this figure legend, the reader is referred to the Web version of this article.)

dynamical spectral functions determined in scattering experiments.

2.2. Application to tellurium dioxide

These features will be discussed in the context of DFT-derived phonon (Fig. 2a) and electron (Fig. 2b) bands and inelastic neutron scattering (INS) measurements for an archetypal chiral material – alpha phase tellurium dioxide (α-TeO_2) with space group $P4_12_12$ [43,44] – which has a record negative linear compressibility [45,46], non-linear optical properties [47–49], multiple twist axes, and, as we demonstrate here, anomalous vibrational spectral features. In particular, we examine the chiral 4_1 c-axis (0, 0, z) (see Fig. 1a). We interchange the terms 'twist' and 'chiral' in structurally chiral materials, but strictly use 'twist' for materials with inversion symmetry, *e.g.*, wurtzite GaN and rutile SnO_2. The primitive unit cell of α-TeO_2, with a and c tetragonal lattice parameters, is comprised of four formula units belonging to layers related by the screw operation: $\pi/2$ rotation with $c/4$ translation (coupled with fractional translations along a and b axes depending on the rotation axis) giving quantum number range $l = \{0,1,2,3\}$ in Eq. (1). In this twist formalism, a single three-atom subunit (*e.g.*, at $n_h = 0$ in Fig. 1a) is the new crystal basis with $R_h = n_h c/4$ and $\theta_h = n_h\pi/2$, where n_h is an integer label of the layer along the chiral axis. Alternatively, the chiral axis can be defined along a or b with a π rotation, $a/2$ translation, and $R_h = n_h a/2$, $\theta_h = n_h\pi$, and $l = \{0,1\}$ (see SM). We also demonstrate phonon twist dynamics for γ-TeO_2 in the SM.

For α-TeO_2 along the chiral c-axis, Eq. (1) gives nine phonon bands for each $l = \{0,1,2,3\}$, which, combined, give 36 total bands identical to the conventional dynamics, but highlighting that each band carries a pseudoangular momentum with Brillouin zone (BZ) periodicity commensurate with the conventional BZ ($|q| \leq \pi/c$), though four times larger due to the smaller real space description (see Fig. 1b lower panel). Bands of different flavors are shifted by $-2\pi l/c$ ([0,0,-l] in reciprocal lattice units) with respect to the $l = 0$ bands. In the SM, we demonstrate the effect of long-range polar corrections on the phonon bands of TeO_2 (Fig. S3(a)). The long-range polar corrections shift phonon bands in frequency, but do not change the physics described below. For electrons, the twelve conduction bands of α-TeO_2 can be classified into four groups of three bands associated with $l = \{0,1,2,3\}$.

2.3. Experiment

Inelastic neutron scattering was collected using the ARCS and HYSPEC beamlines at the Spallation Neutron Source (SNS) on a 1" × 1/2" × 1/2" single crystal of α-TeO_2 (United Crystals). On HYSPEC, data were collected in the H0L and HK0 planes using incident energies of 15 and 7.5 meV; the crystal was rotated 190° in 1° increments to obtain representative sections. Data at ARCS was collected in the H0L plane using an incident energy of 60 meV. The crystal was rotated 190° in 0.25° increments to obtain the complete scattering pattern. All data were collected at 300 K. Data were analyzed using HORACE to produce slices along specific Q orientations.

3. Results

3.1. Crossings and anti-crossings

Twist dynamics highlights how quasiparticle phases dictate band behaviors such as symmetry-enforced crossings and anti-crossings. First, mixing modes from branches of like twist phase leads to anti-crossing [50,51] (see Fig. S1(a) of the SM), while bands of unlike twist phase ignore each other, *i.e.*, cross (see Fig. 2). Thus, along high symmetry lines in twisted materials, only quasiparticle bands of unlike pseudoangular momenta cross, as demonstrated in Fig. 2a and b. Band anti-crossings, particularly hybridization of low frequency optic bands with heat-carrying acoustic bands, have been linked to enhanced phonon resistance and low thermal conductivity in materials of interest for thermoelectric applications [35,36]. We note that the conventional dynamics gives the same band behaviors, though without the intuitive interpretation provided by the twist dynamics.

At high symmetry points (*e.g.*, Γ-point and zone boundaries) the crossing of bands of different pseudoangular momenta is enforced by their phase relations. For phonons along the chiral c-axis in α-TeO_2, Eq. (1) gives four dynamical matrices differing in phase by $e^{in_h\pi l/2}$. At $q = 0$ the phase factors in the twist dynamical matrices for $l = \{0,1,2,3\}$ are $\{1, e^{in_h\pi/2}, e^{in_h\pi}, e^{in_h\pi 3/2}\}$, respectively. Since the phase factors multiply the same real terms in each Hermitian matrix and $e^{in_h\pi 3/2} = e^{-in_h\pi/2}$ (note that $e^{\pm i2n_h\pi} = 1$), this gives $\overline{D}_{l=1} = \overline{D}^*_{l=3}$, complex conjugate pairs with identical eigenvalues (*i.e.*, bands cross) and complex conjugate eigenvectors. Thus, at the Γ point, the $l = 1$ and $l = 3$ modes are degenerate time-reversal

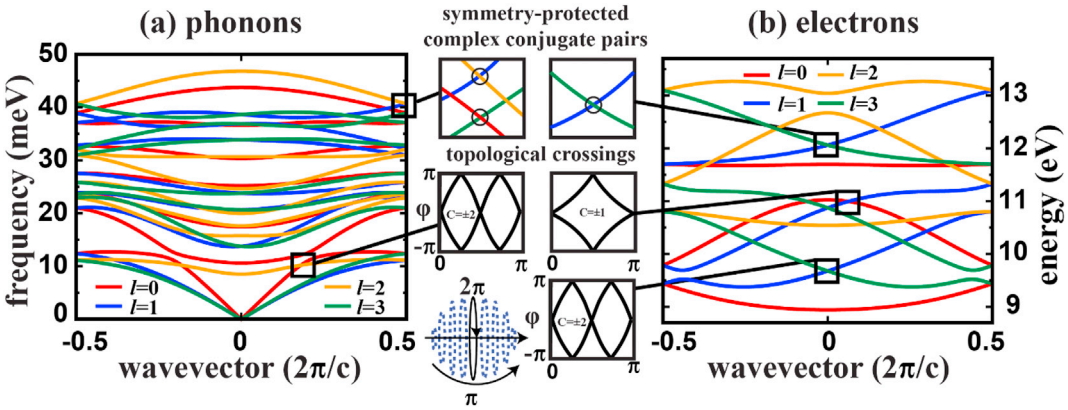

Fig. 2. DFT-derived band structures for α-TeO_2 along the chiral c-axis for **(a)** phonons and **(b)** electrons. Band colors correspond to the labeled pseudoangular momenta l. The top two middle panels focus on symmetry-enforced crossings. The two middle panels and bottom panel show Berry phase winding and Chern classification (C) for different topological band crossings. The cartoon sphere demonstrates the Wilson loop method described in the text. (For interpretation of the references to color in this figure legend, the reader is referred to the Web version of this article.)

partners with opposite slopes (see below). The dynamical matrices describing $l = 0$ and $l = 2$ modes are their own complex conjugates. The situation switches when considering the next BZ center at $q = 2\pi/c$ for which the dynamical matrices for $l = 0$ and $l = 2$ have identical eigenvalues.

At the BZ boundary $q = \pi/c$, the phase factors for $l = \{0,1,2,3\}$ are $\{e^{in_h\pi/4}, e^{i3n_h\pi/4}, e^{i5n_h\pi/4}, e^{i7n_h\pi/4}\}$ ensuring two pairs of identical eigenvalues for $l = \{0,3\}$ and for $l = \{1,2\}$, respectively, because they are complex conjugates. This can be seen in the phonon and electron band structures in Fig. 2. Furthermore, complex conjugate phonon pairs at the BZ boundary are vibrational enantiomers with opposite chirality (see Fig. 1b). On the entire plane perpendicular to the chiral c-axis at $q = \pi/c$ the double screw operation acts like an inversion ($q \rightarrow -q$), which when coupled with time-reversal enforces double degeneracy of the quasiparticle bands [52,53].

Building on the work of Herring [15,16], similar symmetry-enforced degeneracies in electronic energy bands in non-symmorphic space groups were introduced by Michel and Zak [6] in the context of Wyckoff positions and irreducible space group representations. Phase factors in the band representation give complex conjugate pairs of phases for degenerate bands at high symmetry points, analogous to the complex conjugate pairs in our twist dynamical description and underlying symmetry enforced crossings at these points. As pointed out in Ref. [6], these degeneracies lead to 'band connectivity' on the energy axis —bands are continuously connected. Our work further highlights that in the extended zone scheme there is a related 'connectivity' on the momentum axis for bands with a particular pseudoangular momentum (see Fig. S1 of the SM). That is, tracing a band with a particular pseudoangular momentum across multiple zones gives the same connectivity behavior without the abrupt 'folding' at the zone boundaries — a consequence of the phase-shifted relationship of the different energy bands. Furthermore, the Wyckoff positions entering the band representation were shown to carry information about the topological nature of crossings via Berry phase [54]. The present twist dynamics illustrates the topological behavior in terms of pseudoangular momentum (see below).

Twist phases in the chiral dynamics also constrain the slopes of the bands at these symmetry-protected crossings. For phonons, the velocities are real (*i.e.*, $v = v^*$) though they can be defined in terms of derivatives of the dynamical matrices with respect to wavevector, which are complex (see SM). At the Γ point, the velocities for $l = \{0,2\}$ modes are their own complex conjugates and are constrained to be zero (*e.g.*, $v_0 = v_0^* = -v_0 = 0$). On the other hand, $l = 1$ modes are complex conjugates of $l = 3$ modes (time reversal partners); thus, these come in pairs with opposite velocities ($v_1 = v_3^* = -v_3$). Since all bands at the BZ boundary have a complex conjugate pair ($l = \{0,3\}$ and $l = \{1,2\}$), every quasiparticle band has a complex conjugate of opposite slope (see Fig. 2). These symmetry-enforced band behaviors are relevant for topological classifications, *e.g.*, linear and quadratic Weyl nodes (see below).

3.2. Coupling conditions

Another important utility of the twist dynamics is to give insights into quasiparticle couplings in non-symmorphic twisted crystals. Phase interference conditions in interaction matrix elements among quasiparticles lead to pseudoangular momentum conservation along the twist directions. For instance, in lowest order quantum perturbation theory the matrix elements describing the anharmonic interaction of three phonons involve displacement operators that carry phase factors coupling phonon wavevectors to the lattice periodicity: $e^{i(\vec{q}_1\cdot\vec{R}_1)}e^{i(\vec{q}_2\cdot\vec{R}_2)}e^{i(\vec{q}_3\cdot\vec{R}_3)}$. Enforcing translational invariance leads to the interference condition $e^{i(\vec{q}_1+\vec{q}_2+\vec{q}_3)\cdot\vec{R}} = 1$, which, in the twist dynamical scheme, requires that translational and pseudoangular momenta are conserved within a reciprocal lattice vector $\vec{G} = (G, l_G)$: $q_1 + q_2 + q_3 = G$ and $l_1 + l_2 + l_3 = l_G$, where G (continuous) and l_G (integer) are not independent. In α-TeO_2 along the chiral c-axis, the reciprocal lattice vector can be defined with the conventional periodicity ($G = 2\pi m/c$; $l_G = -m$ {mod 4}) or with the twist periodicity ($G = 8\pi m/c$; $l_G = 0$) where m is an integer. Phase interference conditions and pseudoangular momentum conservation occur for all orders of phonon-phonon interactions and similar conditions can be derived for interactions among different quasiparticles (*e.g.*, electron-phonon interactions) of non-symmorphic chiral and achiral crystals. However, the phase interference conditions only apply to the twist axes with their symmetry, not to the entire BZ over which integrations determine transport behaviors. Nonetheless, further insights may yet be developed regarding more general phase interference conditions in non-symmorphic materials.

3.3. Spectral probes

Evidence of chiral phonon behaviors have been observed in infrared absorption [12], inelastic x-ray [55], and metamaterial acoustic [56] measurements, though not understood in terms of the twist dynamics presented here. Like the couplings among quasiparticles, spectral probes that map dynamical structure factors $S(\vec{Q},E)$ [57,58] also obey phase selection rules. $\vec{Q}$ and E are momentum and energy transfer, respectively. Such probes have been invaluable in advancing understanding of fundamental quasiparticle behaviors that underly important functionalities, such as the 'waterfall' effect of zone center optical phonons in PbTe underlying its thermoelectric performance [59]. Here, we use twist dynamics as an effective interpretive tool to understand peculiarities of $S(\vec{Q},E)$ for phonons in single-crystalline α-TeO_2 from INS measurements.

$$S_{1D}(Q,E) = \frac{1}{8N}\sum_{q,j,l}\left|\sum_{hk}\frac{\bar{b}_k}{\sqrt{m_k}}e^{-iQr_{hk}}\left(Q\varepsilon_{q,j,l,k}e^{in_h\pi l/2}e^{iqn_hc/4}\right)\right|^2\frac{1}{\omega_{q,j,l}}\delta(E-\omega_{q,j,l})\delta(Q-q) \quad (2)$$

For phonons in α-TeO_2 along the chiral c-axis, $S(\vec{Q},E)$ can be recast in the twist dynamical formalism as (see SM):

where for simplicity we are working in the extended zone scheme (no reciprocal lattice vectors) and have omitted temperature-dependent Debye-Waller and Bose factors [57,58]. See the SI for derivation of $S_{1D}(Q,E)$ in extended and periodic zone schemes. The '1D' subscript highlights that this dynamical structure factor is projected along a one-dimensional twist axis. In Eq. (2), N is the number of unit cells, $\bar{b}_k$ is the average nuclear scattering length of the kth atom, and $\omega_{q,j,l}$ and $\varepsilon_{q,j,l,k}$ are the frequency and chiral axis

component of the twist eigenvector of the kth atom for phonon mode q,j,l, where j labels the polarization. $r_{hk} = n_h c/4 + \Delta_k$ is the position of atom k in layer h on the chiral axis within the primitive unit cell where the first term locates the layer (see Fig. 1a) and Δ_k locates the atom with respect to this layer. With application of the momentum conserving delta function and rearranging of the exponential terms in Eq. (2), the overall phase of $S_{1D}(Q,E)$ becomes $\sum_{hk} e^{-iQ\Delta_k} e^{in_h \pi l/2}$ (see SM for details). Summing over layers in the primitive unit cell ($n_h = \{0,1,2,3\}$) gives the phase $\sum_k e^{-iQ\Delta_k}(1 + e^{i\pi l/2} + e^{i\pi l} + e^{i3\pi l/2})$. These phase factors determine how the neutrons probe bands with different pseudoangular momenta. For $l = 0$, $1 + e^{i\pi 0/2} + e^{i\pi 0} + e^{i3\pi 0/2} = 4$ and $S_{1D}(Q,E)$ is finite depending on the eigenvectors along the chiral axis. For $l \neq 0$ the combination of phase factors gives zero, *e.g.*, $l = 1$ gives $1 + e^{i\pi/2} + e^{i\pi} + e^{i3\pi/2} = 1 + i - 1 - i = 0$ (see SM for details). In chiral magnetic materials (not discussed here), $S_{1D}(Q,E)$ will behave differently to spin-polarized neutrons via similar rotational phase interference conditions.

Fig. 3a shows INS $S(\vec{Q},E)$ measurements of low frequency acoustic and optic phonons along the chiral c-axis [0, 0, L] of α-TeO_2. Fig. 3b, c, and d give simulated $S(\vec{Q},E)$ from DFT calculations. Based on the measurement geometry, longitudinal acoustic (LA) modes should be visible, while transverse acoustic (TA) modes should not. However, the slope of the measured 'LA' band changes depending on the BZ sampled, even changing within the same BZ along positive and negative directions. More striking is the lack of spectral weight for acoustic phonons in zone [0, 0, 2] (lower white arrow in Fig. 3a). As demonstrated in Fig. 1b (lower panel) the $l = 0$ bands do not have the periodicity of the standard BZ, but rather carry the twist periodicity – the low frequency $l = 0$ branch switches from an LA band ($-\pi/c < q < \pi/c$) to one of two TA bands ($\pi/c < q < 3\pi/c$) to optic ($3\pi/c < q < 5\pi/c$) [0, 0, 2], then to TA again but with reversed polarity, as seen by the INS probe. We note that spectral weight is seen for $l \neq 0$ modes, albeit weak, both in the measurements and calculations that use finite integration width perpendicular to c* in momentum space, *i.e.*, sample modes off the chiral axis. Another signature of the twist dynamics sampled by the measured data is lack of spectral weight for the complex conjugate pair of a zone boundary acoustic phonon band highlighted by the upper white arrow in Fig. 3a. INS data for α-TeO_2 along the chiral a-axis and other interesting cuts are presented in the SM. Observed variations in $S(\vec{Q},E)$ among Brillouin zones in twisted non-symmorphic materials are naturally understood through the lens of the phase dynamics presented here.

3.4. Topological crossings

Quasiparticle twist dynamics also provides useful insights into the characterization of topological properties of chiral materials. Topological insulators are often good thermoelectrics (*e.g.*, Bi_2Te_3 [37]) and topological Weyl phonons have been linked to low thermal conductivity and enhanced thermoelectric behavior in TaSb [38]. Since chiral materials lack inversion symmetry, they are natural candidates for hosting topological quasiparticle physics (*e.g.*, band inversion, protected surface states, Weyl physics) as has been recently explored for electronic bands [20,21,60] and phonon bands [24,61–63]. We find signatures of topological electron and phonon band crossings in α-TeO_2 inferred by analysis of calculations of geometric phase accumulation and resulting Berry phase using the Wilson loop method [62–65]: $\varphi_{Berry} = -\mathrm{Im}[\ln \prod_{m=0}^{N-1} \langle \psi_m | \psi_{m+1} \rangle]$ where ψ_m is the electronic wavefunction or phonon eigenvector calculated at point m on a loop in the BZ. More specifically, we define a sphere in reciprocal space around each band crossing and define circular loops on its surface with N discretized points (see cartoon in Fig. 2). We plot the Berry phase of each loop ranging from one pole of the sphere to the other and examine the phase winding.

Phase windings and resulting band Chern numbers [62–65] are shown in Fig. 2 for different electron and phonon band crossings in α-TeO_2 along the chiral c-axis. Empirically, we find that symmetry-enforced crossings of $l = \{1,3\}$ bands at the Γ point have $\pm 4\pi$ winding, implying these bands carry Chern number $C = \pm 2$. As discussed above, these quasiparticle bands have opposite linear slopes; however, approaching the Γ point along the x or y directions, these bands have symmetry-imposed quadratic dispersion with zero slope at the crossing point, a characteristic of

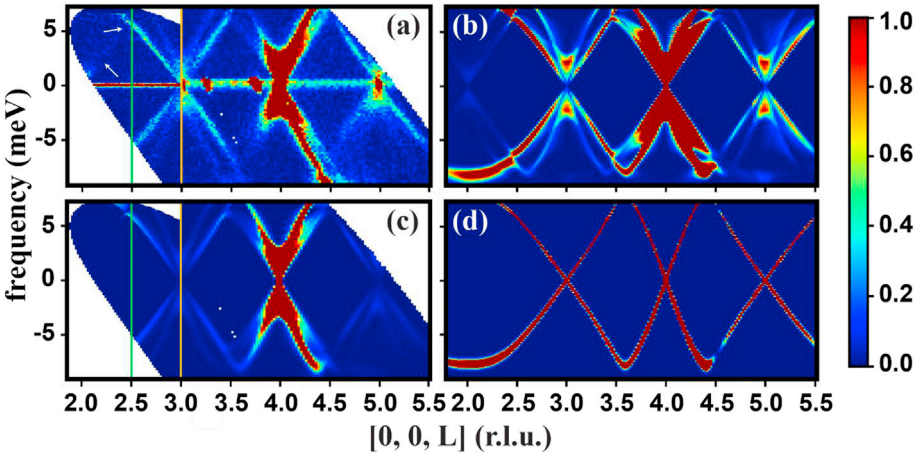

Fig. 3. Dynamical structure factor $S(\vec{Q},E)$ for α-TeO_2 phonons along the chiral c-axis [0, 0, L] longitudinal cut. **(a)** Measured INS data integrated at $-0.12 < \zeta, \eta < 0.12$ in (ζ, 0, 0) and (0, η, 0), **(b)** DFT simulation with integration and intensity scaled to show weak phonons originating from [0, 0, 2], **(c)** DFT simulation with same integration and range as measured data in **(a)**, and **(d)** DFT simulation without integration. Details of the simulations are given in the SM. Data left of the yellow lines in **(a)** and **(c)** use a 7.5 meV incident energy, while to the right use a 15 meV incident energy. The green line designates a BZ boundary, while the upper white arrow highlights the non-zero slope of the acoustic branch at this boundary and missing complex conjugate pair. The lower white arrow highlights the lack of intensity of acoustic phonons originating from [0, 0, 2] that are forbidden by twist symmetry. All intensities are scaled to best visualize the features of interest. (For interpretation of the references to color in this figure legend, the reader is referred to the Web version of this article.)

quadratic Weyl nodes [8]. Symmetry-enforced crossings of $l = \{0,3\}$ and $l = \{1,2\}$ at the BZ boundary are topologically trivial, $C = 0$. As discussed above, symmetry-enforced crossings underlie energy band 'connectivity' [6], which "*can be moved but not removed because they are a consequence of symmetry and topology*" [66]. Between Γ and the BZ boundary, crossings involving bands $l = \{1,3\}$ and $l = \{0,2\}$ also have ±2 Chern number with quadratic dispersions perpendicular to the chiral axis. Crossings corresponding to $l = \{0,3\}$, $l = \{2,3\}$, and $l = \{1,2\}$ at arbitrary points along the *c*-axis carry Chern number $C\pm1$ and have linear dispersions perpendicular to this axis − linear Weyl nodes [62]. Along the chiral *a*-axis all branch crossings at arbitrary wavevector give $C = \pm1$, while at the π/a zone boundary the enforced crossings are again topologically trivial.

4. Summary

To summarize, the twist quasiparticle dynamics developed here sheds light on the roles of twist symmetries and phase interference conditions underlying a variety of behaviors in chiral and achiral non-symmorphic materials. This can be applied to electrons, phonons, and other quasiparticles, from DFT to model Hamiltonian descriptions, to build insights into interactions, symmetry-protected and topological band crossings, and dynamical structure factors probed in scattering experiments. We specifically demonstrated these behaviors for electrons and phonons in chiral α-TeO_2, particularly highlighting twist dynamics related to inelastic neutron scattering measurements of its phonon dispersion. Application of this twist dynamics to quasiparticles in the large variety of twisted non-symmorphic materials will build novel insights into their behaviors and functionalities and guide the conception of new experimental techniques to study them. More particularly, enhanced understanding of quantum phase interference conditions will derive insights into quasiparticle interactions that govern electronic and thermal transport behaviors in complex unit cell materials of particular interest for thermoelectric and thermal management applications.

Declaration of competing interest

The authors declare that they have no known competing financial interests or personal relationships that could have appeared to influence the work reported in this paper.

Acknowledgements

This work was supported by the US Department of Energy, Office of Science, Office of Basic Energy Sciences, Material Sciences and Engineering Division. Computational resources were provided by the National Energy Research Scientific Computing Center (NERSC), a DOE Office of Science User Facility supported by the Office of Science of the US Department of Energy under Contract No. DE-AC02-05CH11231. A portion of this research (INS at HYSPEC and ARCS) used resources at the Spallation Neutron Source, a DOE Office of Science User Facility operated by Oak Ridge National Laboratory.

Author contributions

R.P.H. and L.L. initiated this work. R.J., L.L., T.P., and C.A.P. contributed phonon calculations. S.T. contributed electronic band structure calculations. Y.Q.C. provided dynamical structure factor simulations. R.P.H., D.H.M., B.W., D.L.A., and M.E.M. performed inelastic neutron scattering experiments and data analysis. R.J., L.L., R.P.H., T.P., S.T., B.W., and M.E.M. contributed to manuscript development. Dr. Junjie Zhang is acknowledged for help during neutron data acquisition.

Data and materials availability

Details of the calculations, materials, and measurements are provided in the SM. Further calculation and measurement data are available upon reasonable email request.

Appendix A. Supplementary data

Supplementary data to this article can be found online at https://doi.org/10.1016/j.mtphys.2021.100548.

References

[1] J.K. Barton, Metals and DNA: molecular left-handed complements, Science 233 (1986) 727–734, https://doi.org/10.1126/science.3016894.
[2] Z. Haijun, O. Zhong-can, Bending and twisting elasticity: a revised Marko-Siggia model on DNA chirality, Phys. Rev. E 58 (1998) 4816, https://doi.org/10.1103/PhysRevE.58.4816.
[3] Y. Cao, V. Fatemi, S. Fang, K. Watanabe, T. Taniguchi, E. Kaxiras, P. Jarillo-Herrero, Unconventional superconductivity in magic-angle graphene superlattices, Nature 556 (2018) 43–50, https://doi.org/10.1038/nature26160.
[4] H.S. Arora, R. Polski, Y. Zhang, A. Thomson, Y. Choi, H. Kim, Z. Lin, I.Z. Wilson, X. Xu, J. Chu, K. Watanabe, T. Taniguchi, J. Alicea, S. Nadj-Perge, Superconductivity in metallic twisted bilayer graphene stabilized by WSe_2, Nature 583 (2020) 379–384, https://doi.org/10.1038/s41586-020-2473-8.
[5] H.D. Flack, Chiral and achiral crystal structures, Helv. Chim. Acta 86 (2003) 905–921, https://doi.org/10.1002/hlca.200390109.
[6] L. Michel, J. Zak, Connectivity of energy bands in crystals, Phys. Rev. B 59 (1999) 5998, https://doi.org/10.1103/PhysRevB.59.5998.
[7] M. Nespolo, M. Aroyo, B. Souvignier, Crystallographic shelves: space-group hierarchy explained, J. Appl. Crystallogr. 51 (2018) 1481–1491, https://doi.org/10.1107/s1600576718012724.
[8] G.S. Chirikjian, K. Ratnayake, S. Sajjadi, Decomposition of Sohncke space groups into products of Bieberbach and symmorphic parts, Z. Kristallogr. 230 (2015) 719–741, https://doi.org/10.1515/zkri-2015-1859.
[9] M. Damnjanovic, I. Bozovic, N. Bozovic, Selection rules for polymers and quasi one dimensional crystals. II. Kronecker products for the line groups isogonal to D_n, J. Phys. Math. Gen. 17 (1984) 747–756, https://doi.org/10.1088/0305-4470/17/4/016.
[10] T. Pandey, C.A. Polanco, V.R. Cooper, D.S. Parker, L. Lindsay, Symmetry-driven phonon chirality and transport in one-dimensional and bulk Ba_3N-derived materials, Phys. Rev. B 98 (2018) 241405, https://doi.org/10.1103/PhysRevB.98.241405.
[11] L. Lindsay, D.A. Broido, N. Mingo, Lattice thermal conductivity of single-walled carbon nanotubes: beyond the relaxation time approximation and phonon-phonon scattering selection rules, Phys. Rev. B 80 (2009) 125407, https://doi.org/10.1103/PhysRevB.80.125407.
[12] H. Zhu, J. Yi, M. Li, J. Xiao, L. Zhang, C. Yang, R.A. Kaindl, L. Li, Y. Wang, X. Zhang, Observation of chiral phonons, Science 359 (2018) 579–582, https://doi.org/10.1126/science.aar2711.
[13] L. Zhang, Q. Niu, Chiral phonons at high-symmetry points in monolayer hexagonal lattices, Phys. Rev. Lett. 115 (2015) 115502, https://doi.org/10.1103/PhysRevLett.115.115502.
[14] H. Chen, W. Wu, J. Zhu, S.A. Yang, L. Zhang, Propagating chiral phonons in three-dimensional materials, Nano Lett. 21 (2021) 3060–3065, https://doi.org/10.1021/acs.nanolett.1c00236.
[15] C. Herring, Effect of time-reversal symmetry on energy bands of crystals, Phys. Rev. 52 (1937) 361, https://doi.org/10.1103/PhysRev.52.361.
[16] C. Herring, Accidental degeneracy in the energy bands of crystals, Phys. Rev. 52 (1937) 365, https://doi.org/10.1103/PhysRev.52.365.
[17] A. König, N.D. Mermin, Electronic level degeneracy in nonsymmorphic periodic or aperiodic crystals, Phys. Rev. B 56 (1997) 13607, https://doi.org/10.1103/PhysRevB.56.13607.
[18] H. Watanabe, H.C. Po, M.P. Zaletel, A. Vishwanath, Filling-enforced gaplessness in band structures of the 230 space groups, Phys. Rev. Lett. 117 (2016): 096404, https://doi.org/10.1103/PhysRevLett.117.096404.
[19] Y.X. Zhao, A.P. Schnyder, Nonsymmorphic symmetry-required band crossings in topological semimetals, Phys. Rev. B 94 (2016) 195109, https://doi.org/10.1103/PhysRevB.94.195109.
[20] G. Chang, B.J. Wieder, F. Schindler, D.S. Sanchez, I. Belopolski, S. Huang, B. Singh, D. Wu, T. Chang, T. Neupert, S. Xu, H. Lin, M.Z. Hasan, Topological quantum properties of chiral crystals, Nat. Mater. 17 (2018) 978–985, https://doi.org/10.1038/s41563-018-0169-3.
[21] C. Fang, L. Fu, New classes of three-dimensional topological crystalline insulators: nonsymmorphic and magnetic, Phys. Rev. B 91 (2015) 161105, https://doi.org/10.1103/PhysRevB.91.161105.
[22] K. Shiozaki, M. Sato, K. Gomi, Topology of nonsymmorphic crystalline

insulators and superconductors, Phys. Rev. B 93 (2016) 195413, https://doi.org/10.1103/PhysRevB.93.195413.
[23] M. Yao, K. Manna, Q. Yang, A. Fedorov, V. Voroshnin, B.V. Schwarze, J. Hornung, S. Chattopadhyay, Z. Sun, S.N. Guin, J. Wosnitza, H. Borrmann, C. Shekhar, N. Kumar, J. Fink, Y. Sun, C. Felser, Observation of giant spin-split Fermi-arc with maximal Chern number in the chiral topological semimetal PtGa, Nat. Commun. 1 (2020) 11, https://doi.org/10.1038/s41467-020-15865-x.
[24] X. Xu, W. Zhang, J. Wang, Lifa Zhang, Topological chiral phonons in center-stacked bilayer triangle lattices, J. Phys. Condens. Matter 30 (2018) 225401, https://doi.org/10.1088/1361-648x/aabf5e.
[25] D.S. Sanchez, I. Belopolski, T.A. Cochran, X. Xu, J. Yin, G. Chang, W. Xie, K. Manna, V. Süß, C. Huang, N. Alidoust, D. Multer, S.S. Zhang, N. Shumiya, X. Wang, G. Wang, T. Chang, C. Felser, S. Xu, S. Jia, H. Lin, M.Z. Hasan, Topological chiral crystals with helicoid-arc quantum states, Nature 567 (2019) 500–505, https://doi.org/10.1038/s41586-019-1037-2.
[26] Z. Huang, Z. Chen, B. Zheng, H. Xu, Three-terminal Weyl complex with double surface arcs in a cubic lattice, npj Comput. Mater. 6 (2020) 87, https://doi.org/10.1038/s41524-020-00354-y.
[27] N.B.M. Schröter, D. Pei, M.G. Vergniory, Y. Sun, K. Manna, F. de Juan, Jonas A. Krieger, V. Süss, M. Schmidt, P. Dudin, B. Bradlyn, T.K. Kim, T. Schmitt, C. Cacho, C. Felser, V.N. Strocov, Y. Chen, Chiral topological semimetal with multifold band crossings and long Fermi arcs, Nat. Phys. 15 (2019) 759–765, https://doi.org/10.1038/s41567-019-0511-y.
[28] Y.J. Jin, Z.J. Chen, X.L. Xiao, H. Xu, Tunable double Weyl phonons driven by chiral point group symmetry, Phys. Rev. B 103 (2021) 104101, https://doi.org/10.1103/PhysRevB.103.104101.
[29] M.Z. Hasan, G. Chang, I. Belopolski, G. Bian, S. Xu, J. Yin, Weyl, Dirac and high-fold chiral fermions in topological quantum matter, Nat. Rev. Mater. (2021), https://doi.org/10.1038/s41578-021-00301-3.
[30] H. Peng, N. Kioussis, G.J. Snyder, Elemental tellurium as a chiral p-type thermoelectric material, Phys. Rev. B 89 (2014) 195206, https://doi.org/10.1103/PhysRevB.89.195206.
[31] S.-J. Kim, S. Hu, C. Uher, T. Hogan, B. Huang, J.D. Corbett, M.G. Kanatzidis, Structure and thermoelectric properties of Ba_6Ge_{25-x}, $Ba_6Ge_{23}Sn_2$, and $Ba_6Ge_{22}In_3$: Zintl phases with a chiral clathrate structure, J. Solid State Chem. 153 (2000) 321, https://doi.org/10.1006/jssc.2000.8777.
[32] W.D.C.B. Gunatilleke, R. Juneja, O.P. Ojo, A.F. May, H. Shin, L. Lindsay, G.S. Nolas, Intrinsic anharmonicity and thermal properties of ultralow thermal conductivity $Ba_6Sn_6Se_{13}$, Phys. Rev. Mater. 5 (2021): 085002, https://doi.org/10.1103/PhysRevMaterials.5.085002.
[33] T. Pandey, A.S. Nissimagoudar, A. Mishra, A.K. Singh, Ultralow thermal conductivity and high thermoelectric figure of merit in mixed valence In_5X_5Br (X=S, and Se) compounds, J. Mater. Chem. A 8 (2020) 13812, https://doi.org/10.1039/d0ta03841e.
[34] Y.-L. Pei, J. He, J.-F. Li, F. Li, Q. Liu, W. Pan, C. Barreteau, D. Berardan, N. Drogoe, L.-D. Zhao, High thermoelectric performance of oxyselenides: intrinsically low thermal conductivity of Ca-doped BiCuSeO, npj Asia Mater 5 (2013) e47, https://doi.org/10.1038/am.2013.15.
[35] W. Li, N. Mingo, Ultralow lattice thermal conductivity of the fully filled skutterudite $YbFe_4Sb_{12}$ due to the flat avoided-crossing filler modes, Phys. Rev. B 91 (2015) 144304, https://doi.org/10.1103/PhysRevB.91.144304.
[36] M. Christensen, A.B. Abrahamsen, N.B. Christensen, F. Juranyi, N.H. Andersen, K. Lefmann, J. Andreasson, C.R.H. Bahl, B.B. Iversen, Avoided crossing of rattler modes in thermoelectric materials, Nat. Mater. 7 (2008) 811, https://doi.org/10.1038/nmat2273.
[37] N. Xu, Y. Xu, J. Zhu, Topological insulators for thermoelectrics, npj Quantum Mater 2 (2017) 51, https://doi.org/10.1038/s41535-017-0054-3.
[38] S. Singh, Q.-S. Wu, C. Yue, A.H. Romero, A.A. Soluyanov, Topological phonons and thermoelectricity in triple-point metals, Phys. Rev. Mater. 2 (2018) 114202, https://doi.org/10.1103/PhysRevMaterials.2.114204.
[39] V.N. Popov, V.E. Van Doren, M. Balkanski, Elastic properties of single-walled carbon nanotubes, Phys. Rev. B 61 (2000) 3078, https://doi.org/10.1103/PhysRevB.61.3078.
[40] A.A. Mostofi, J.R. Yates, Y.-S. Lee, I. Souza, D. Vanderbilt, N. Marzari, Wannier90: a tool for obtaining maximally-localised Wannier functions *Comp*, Phys. Comm. 178 (2008) 685, https://doi.org/10.1016/j.cpc.2007.11.016.
[41] W. Kohn, L.J. Sham, Self-consistent equations including exchange and correlation effects, Phys. Rev. 140 (1965) A1133, https://doi.org/10.1103/PhysRev.140.A1133.
[42] L.J. Sham, M. Schlüter, Density-functional theory of the energy gap, Phys. Rev. Lett. 51 (1983) 1888, https://doi.org/10.1103/PhysRevLett.51.1888.
[43] M. Ceriotti, F. Pietrucci, M. Bernasconi, Ab initio study of the vibrational properties of crystalline TeO_2: the α, β, and γ phases, Phys. Rev. B 73 (2006) 104304, https://doi.org/10.1103/PhysRevB.73.104304.
[44] I. Sergueev, K. Glazyrin, M.G. Hermann, P. Alexeev, H.-C. Wille, O. Leupold, A.F. May, T. Pandey, L.R. Lindsay, K. Friese, R.P. Hermann, High-pressure nuclear inelastic scattering with backscattering monochromatization, J. Synchrotron Radiat. 26 (2019) 1592–1599, https://doi.org/10.1107/S1600577519008853.
[45] A.B. Cairns, A.L. Goodwin, Negative linear compressibility, Phys. Chem. Chem. Phys. 17 (2015) 20449, https://doi.org/10.1039/C5CP00442J.
[46] T.G. Worlton, R.A. Beyerlein, Structure and order parameters in the pressure-induced continuous transition in TeO_2, Phys. Rev. B 12 (1975) 1899, https://doi.org/10.1103/PhysRevB.12.1899.
[47] Y. Ohmachi, N. Uchida, Temperature dependence of elastic, dielectric, and piezoelectric constants in TeO_2 single crystals, J. Appl. Phys. 41 (1970) 2307–2311, https://doi.org/10.1063/1.1659223.
[48] P.A. Thomas, The crystal structure and absolute optical chirality of paratellurite, α-TeO_2, J. Phys. C 21 (1988) 4611–4627, https://doi.org/10.1088/0022-3719/21/25/009.
[49] N. Berkaïne, E. Orhan, O. Masson, P. Thomas, J. Junquera, Nonlinear optical properties of TeO_2 crystalline phases from first principles, Phys. Rev. B 83 (2011) 245205, https://doi.org/10.1103/PhysRevB.83.245205.
[50] J. von Neumann, E.P. Wigner, On the Behavior of Eigenvalues in Adiabatic Processes, the Collected Works of Eugene Paul Wigner, Springer, Berlin, 1993, pp. 294–297, https://doi.org/10.1007/978-3-662-02781-3_20.
[51] Yu N. Demkov, P.B. Kurasov, Von Neumann-Wigner theorem: level repulsion and degenerate eigenvalues, Theor. Math. Phys. 153 (2007) 1407–1422, https://doi.org/10.1007/s11232-007-0124-y.
[52] M.Z. Hasan, C.L. Kane, Colloquium: topological insulators, Rev. Mod. Phys. 82 (2010) 3045, https://doi.org/10.1103/RevModPhys.82.3045.
[53] N.P. Armitage, E.J. Mele, Ashvin Vishwanath, Weyl and Dirac semimetals in three-dimensional solids, Rev. Mod. Phys. 90 (2018): 015001, https://doi.org/10.1103/RevModPhys.90.015001.
[54] J. Zak, Berry's phase for energy bands in solids, Phys. Rev. Lett. 62 (1989) 2747, https://doi.org/10.1103/PhysRevLett.62.2747.
[55] H. Li, T. Zhang, A. Said, Y. Fu, G. Fabbris, D.G. Mazzone, J. Zhang, J. Lapano, H.N. Lee, H.C. Lei, M.P.M. Dean, S. Murakami, H. Miao, Observation of a chiral wave function in the twofold-degenerate quadruple Weyl system BaPtGe, Phys. Rev. B 103 (2021) 184301, https://doi.org/10.1103/PhysRevB.103.184301.
[56] X. Ni, M. Weiner, A. Alù, A.B. Khanikaev, Observation of higher-order topological acoustic states protected by generalized chiral symmetry, Nat. Mater. 18 (2019) 113–120, https://doi.org/10.1038/s41563-018-0252-9.
[57] G. Shirane, S.M. Shapiro, J.M. Tranquada, Neutron Scattering with a Triple-Axis Spectrometer, Cambridge University Press, Cambridge, 2002.
[58] Y.Q. Cheng, L.L. Daemen, A.I. Kolesnikov, A.J. Ramirez-Cuesta, Simulation of inelastic neutron scattering spectra using OCLIMAX, J. Chem. Theor. Comput. 15 (2019) 1974–1982, https://doi.org/10.1021/acs.jctc.8b01250.
[59] O. Delaire, J. Ma, K. Marty, A.F. May, M.A. McGuire, M.-H. Du, D.J. Singh, A. Podlesnyak, G. Ehlers, M.D. Lumsden, B.C. Sales, Giant anharmonic phonon scattering in PbTe, Nat. Mater. 10 (2011) 614, https://doi.org/10.1038/nmat3035.
[60] C. Fang, M.J. Gilbert, X. Dai, B.A. Bernevig, Multi-Weyl topological semimetals stabilized by point group symmetry, Phys. Rev. Lett. 108 (2012) 266802, https://doi.org/10.1103/PhysRevLett.108.266802.
[61] B. Peng, Y. Hu, S. Murakami, T. Zhang, B. Monserrat, Topological phonons in oxide perovskites controlled by light, Sci. Adv. 6 (2020) 46, https://doi.org/10.1126/sciadv.abd1618.
[62] Q. Liu, Y. Qian, H. Fu, Z. Wang, Symmetry-enforced Weyl phonons, npj Comput. Mater. 6 (2020), https://doi.org/10.1038/s41524-020-00358-8.
[63] T. Zhang, Z. Song, A. Alexandradinata, H. Weng, C. Fang, L. Lu, Z. Fang, Double-Weyl phonons in transition-metal monosilicides, Phys. Rev. Lett. 120 (2018): 016401, https://doi.org/10.1103/PhysRevLett.120.016401.
[64] D. Vanderbilt, Berry Phases in Electronic Structure Theory: Electric Polarization, Orbital Magnetization and Topological Insulators, Cambridge University Press, Cambridge, 2018.
[65] R. Yu, X.L. Qi, A. Bernevig, Z. Fang, X. Dai, Equivalent expression of Z2 topological invariant for band insulators using the non-Abelian Berry connection, Phys. Rev. B 84 (2011): 075119, https://doi.org/10.1103/PhysRevB.84.075119.
[66] L. Michel, J. Zak, Elementary energy bands in crystals are connected, Phys. Rep. 341 (2001) 377, https://doi.org/10.1016/S0370-1573(00)00093-4.